Hydrolysis Catalysis of *Miscanthus* Xylan to Xylose Using Weak-Acid Surface Sites

Po-Wen Chung,* Alexandre Charmot, Olayinka A. Olatunji-Ojo, Kathleen A. Durkin, Alexander Katz*

Department of Chemical and Biomolecular Engineering, University of California, Berkeley, CA 94720, U.S.A

**corresponding authors: cedricchung@berkeley.edu; katz@cchem.berkeley.edu*

Supporting Information

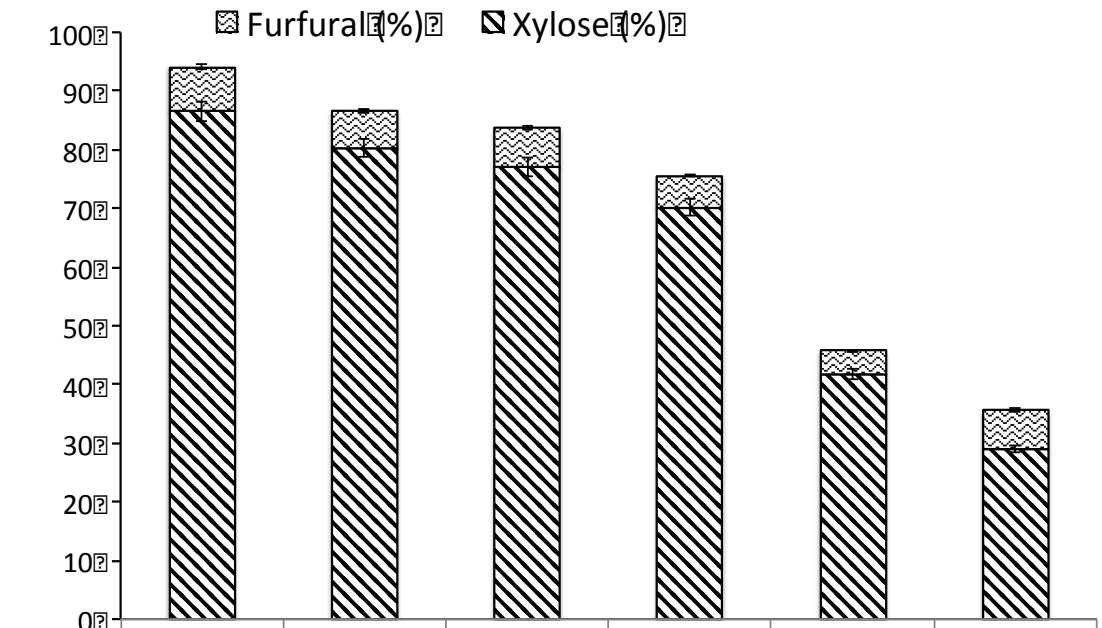

	HSO3-MCN	HT1-HSO3-MCN	HT5-HSO3-MCN	COOH-MCN	MCN	Xylan solution
Furfural (%)	7.5	6.1	6.7	5.5	4	6.6
Xylose (%)	86.6	80.4	77	70.1	41.7	29

Figure S1. Hydrolysis yield of xylan using mesoporous carbon materials in the presence of sodium acetate buffer, which is expressed on the basis of total xylose equivalents content of the *Miscanthus* extract. This extract (before hydrolysis catalysis conditions) contains a slight amount of xylose corresponding to 9.7% xylose yield.

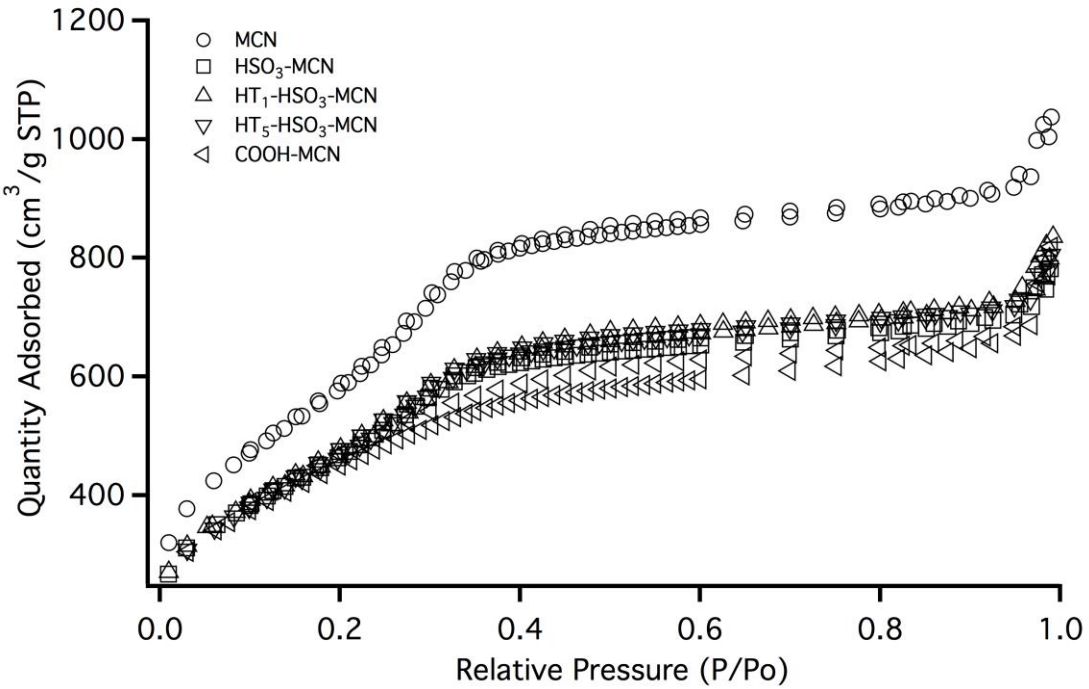

Figure S2. Nitrogen adsorption isotherms for MCN, HSO_3-MCN, HT_1-HSO_3-MCN, HT_5-HSO_3-MCN and COOH-MCN.

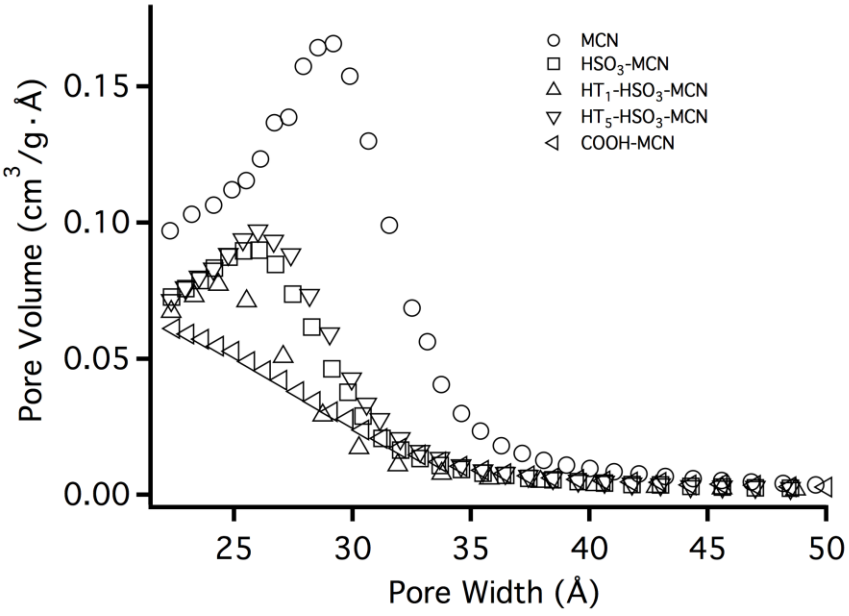

Figure S3. Pore size distributions for MCN, HSO_3-MCN, HT_1-HSO_3-MCN, HT_5-HSO_3-MCN and COOH-MCN.

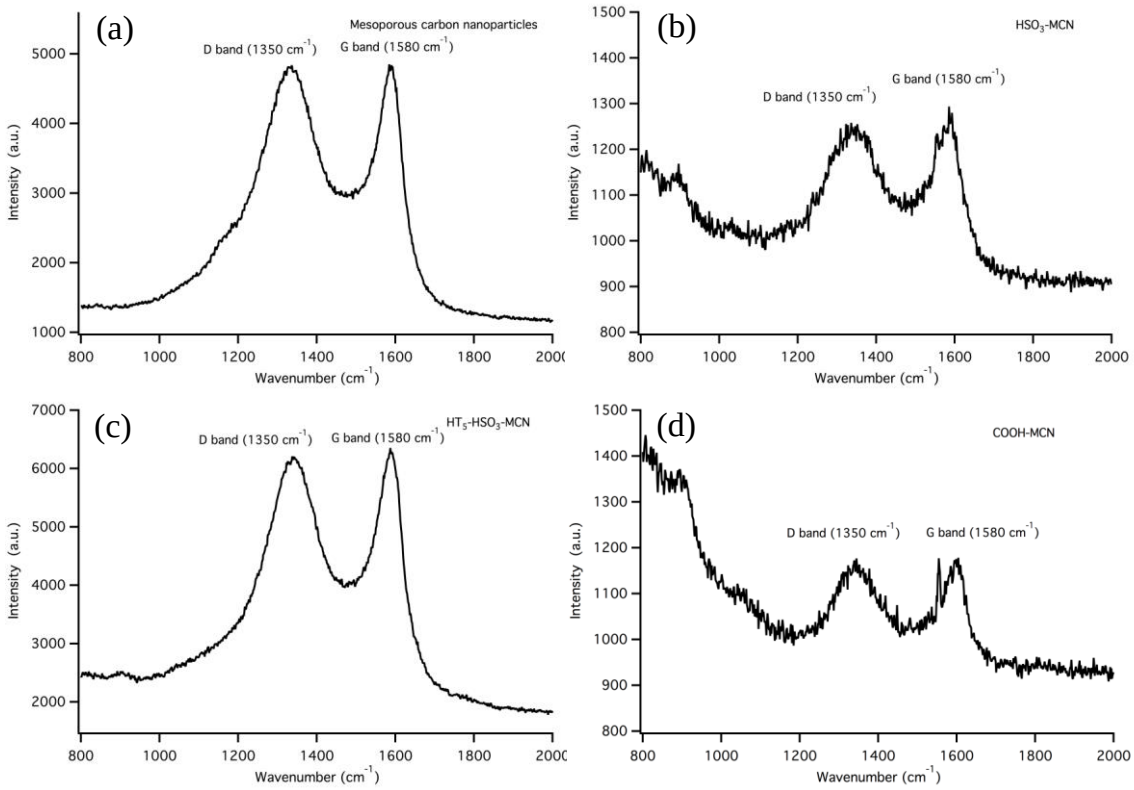

Figure S4. Raman spectroscopy for MCN, HSO_3-MCN, HT_5-HSO_3-MCN and COOH-MCN.

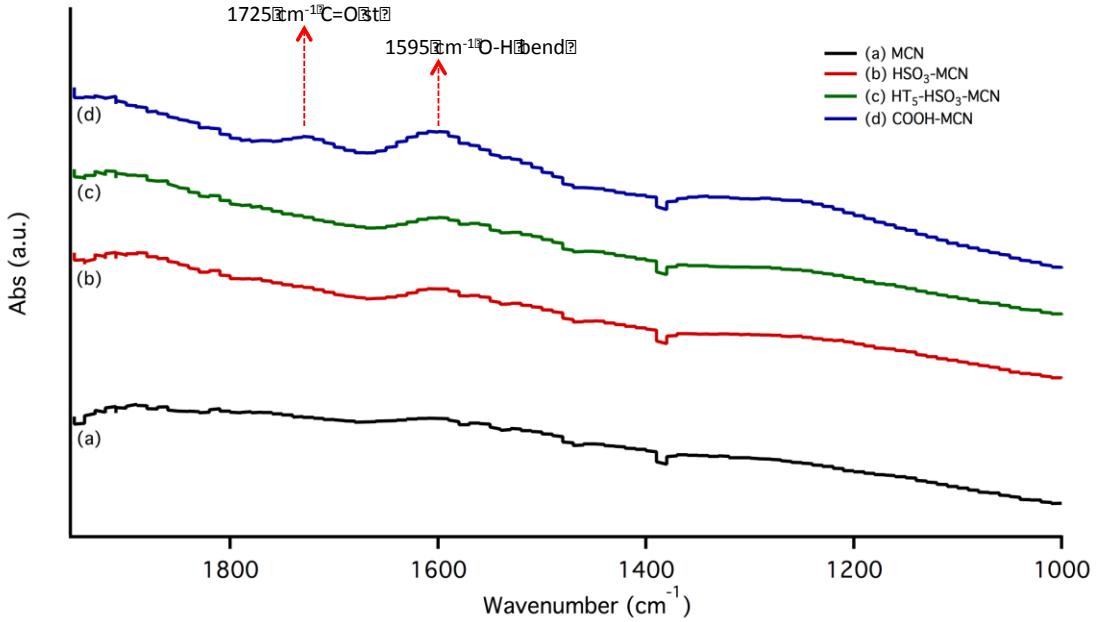

Figure S5. ATR-FTIR spectra of (a) MCN (black), (b) HSO_3-MCN (red), (c) HT_5-HSO_3-MCN (green) and (d) COOH-MCN (blue). Regions corresponding to C=O stretches and the band for O-H bending are labeled.

Table S1. Quantitative scan of trace metals from xylan extract

Element	Concentration (ppm)
Al	1
Ca	28
Fe	3
K	78
Mg	13
Mn	4
Na	1
Nb	1
P	19
Se	1
Si	115
Tl	1
Zn	1

Computational Study

Method

Molecular dynamics simulation was conducted using MacroModel and Desmond as implemented in the Maestro 9.6 software. An initial benchmark study to confirm choice of methodology for the 15 DP units (1→4)-β-D-xylan was conducted by calculating the radius of gyration of (1→4)-α-D-glucan and (1→4)-β-D-glucan (degree of polymerization (DP) = 5 and 10 repeat units of glucose) and comparing to literature experimental and calculated values. For these latter two molecules, initial stochastic dynamics simulation using MacroModel with the OPLS-2005 force field in implicit solvent (water) for 100 ns at 300 K with maximum iteration of 2500, timestep of 1.5 fs and an equilibration time of 1.0 ps was conducted, and the SHAKE procedure was specified for bonds to hydrogen.

Replica exchange molecular dynamics (REMD) simulations as implemented in Desmond were also used as a benchmarking tool. Six replicas at 50 ns each (total of 300 ns) with a temperature range of 300 – 600 K distributed quadratically between the replicas in a NVT ensemble were used. The simulation box was a cubic box with a 10^3 Å buffer. A stochastic dynamics simulation in MacroModel utilizing the final geometry from the Desmond replica exchange simulation was conducted. The SHAKE procedure was specified for bonds to hydrogen. The OPLS-2005 force field in implicit solvent (water) for 10 ns at 300 K with maximum iteration of 2500, timestep of 1.5 fs and an equilibration time of 1.0 ps was used. A molecular dynamics simulation in Desmond with the solvent explicitly described using the SPC water model in a 10^3 Å cubic box was used for the 15 DP unit (degree of polymerization represented by 15 xylose repeat units)

(1→4)-β-D-xylan. The difference between the implicitly and explicitly solvated models was negligible. The radius of gyration was calculated using the provided script in the Schrödinger software with the formalism:

$$R^2 = \frac{1}{N} * \sum (r_i - r_{mean})^2$$

Results

For the MacroModel dynamics simulation, the radius of gyration for the final 300 snapshots was averaged while the final 200 snapshots were averaged for the replica exchange simulations. The stochastic dynamics simulation resulted in a fairly linear structure, with limited folding for the 5 and 10 DP (1→4)-α-D-glucan. Replica exchange molecular dynamics simulation resulted in a coiled structure (Figure1). The final geometry from the REMD calculation was then placed in implicit solvent to account for solvent effects. In the span of the dynamics simulation (10 ns), the glucan and xylan structures unfold to an almost linear structure as observed in the initial stochastic dynamics simulation (Figures 2 and 3). The calculated radius of gyration using the 10 ns MD simulation from MacroModel for the α and β structures agree to within 0.3 Å (Table 1). The radius of gyration for the (1→4)-β-D-xylan reported in Table 1 is from the explicitly solvated simulation. Figures 1-4 illustrates the different geometries observed during the course of simulation.

Table S2. Radii of gyration of polysaccharides of varying DP in aqueous solution.

Structure (DP)	This work	Previous Experimental[a]	Previous Calculation[a]
(1→4)-α-D-glucan (5)	6.31 Å	6.15 Å	6.04 Å
(1→4)-α-D-glucan (10)	10.41 Å	10.11 Å	8.83 Å
(1→4)-β-D-glucan (5)	7.65 Å	-	7.61 Å
(1→4)-β-D-glucan (10)	14.47 Å	-	14.7 Å
(1→4)-β-D-xylan (15)	20.47 Å	-	-

[a]Previous experimental and calculation results were obtained from the book of "*Polysaccharrides: Structural Diversity and Functional Versatility*" Dumitriu, S. CRC Press, 2005

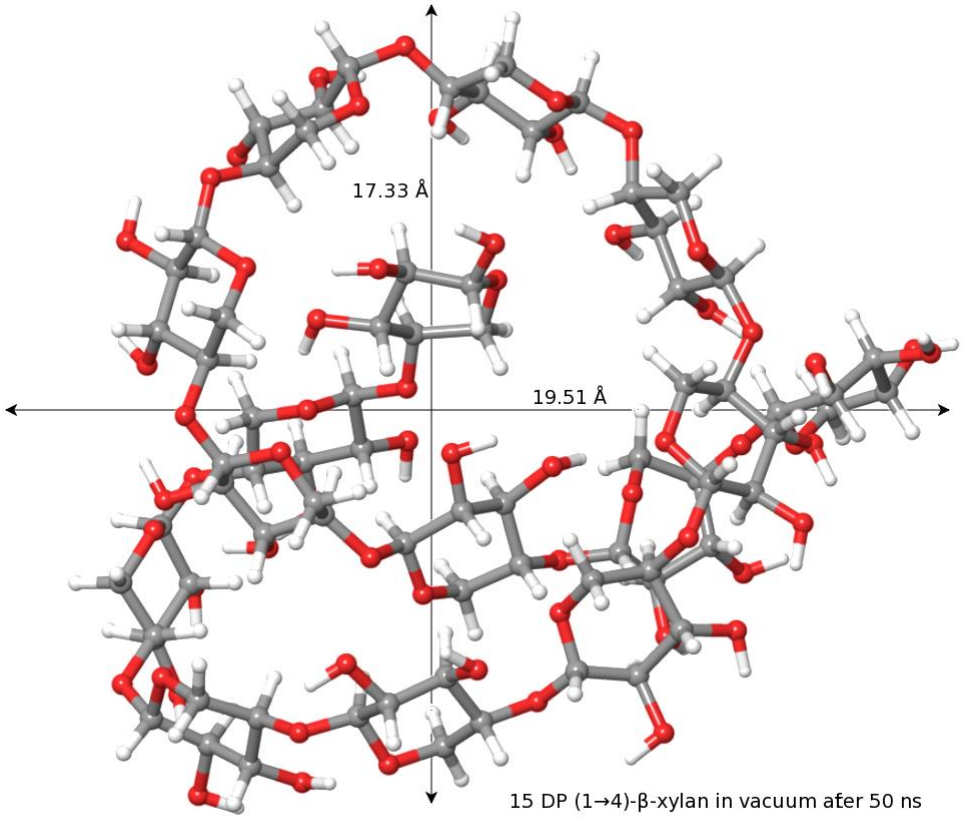

Figure S6. Replica Exchange Molecular Dynamics (REMD) structure of the 15 DP units (1→4)-β-D-xylan in vacuum after 50 ns.

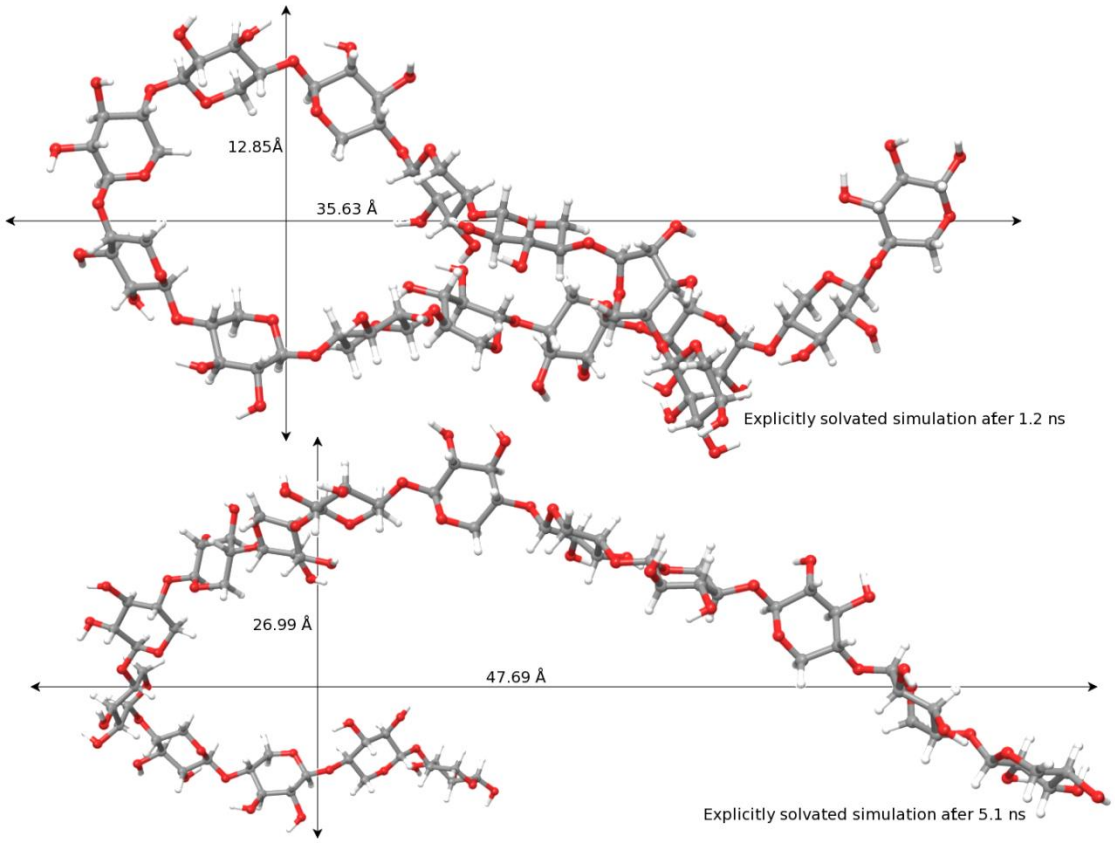

Figure S7. Molecular dynamics simulation structures of the 15 DP units (1→4)-β-D-xylan in water after 1.2 and 5.1 ns respectively. Water molecules are excluded for clarity.

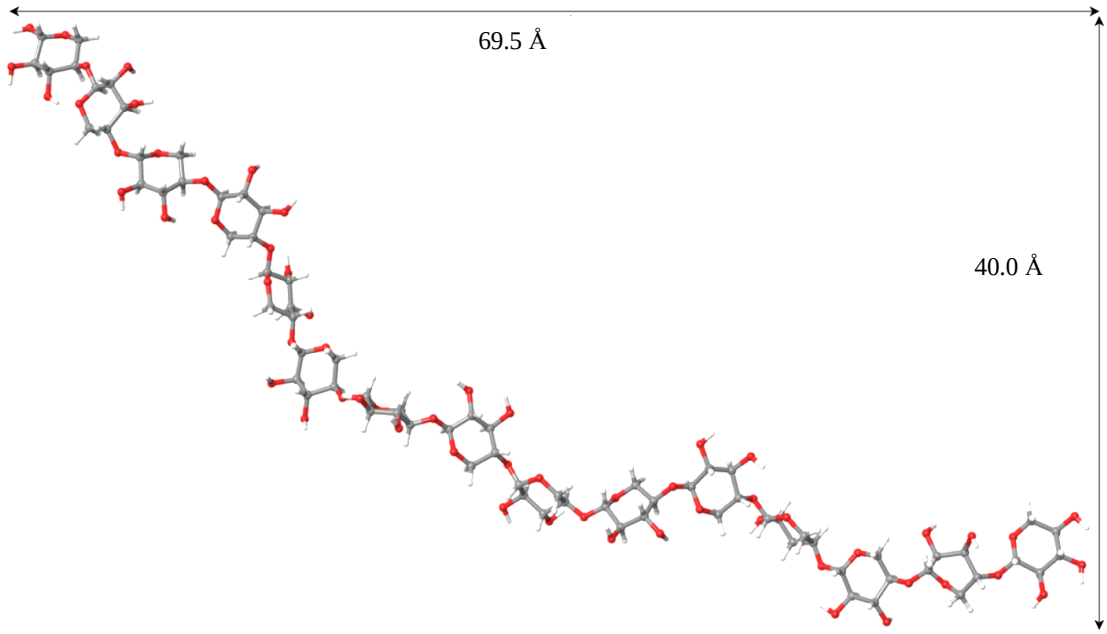

Figure S8. Molecular dynamics simulation structures of the 15 DP units (1→4)-β-D-xylan in water after 10 ns. Water molecules are excluded for clarity.

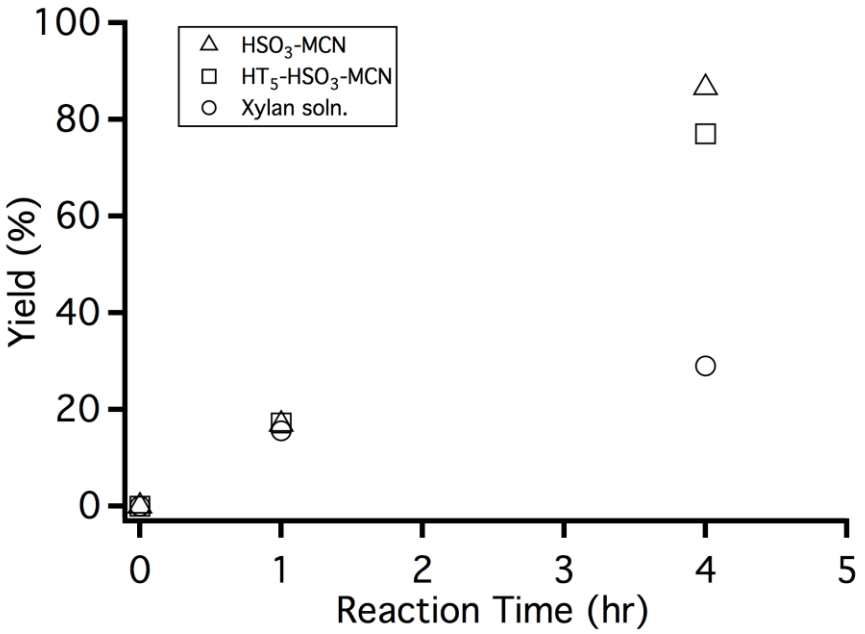

Figure S9. Initial rate of hydrolysis of xylan using mesoporous carbon materials shows a uniform rate of xylose release in the complex reaction scheme involving long-chain xylans becoming converted to xylose. Experimental details: same as in experimental portion of manuscript except where xylan extract rather than buffer solution was used as reaction medium.

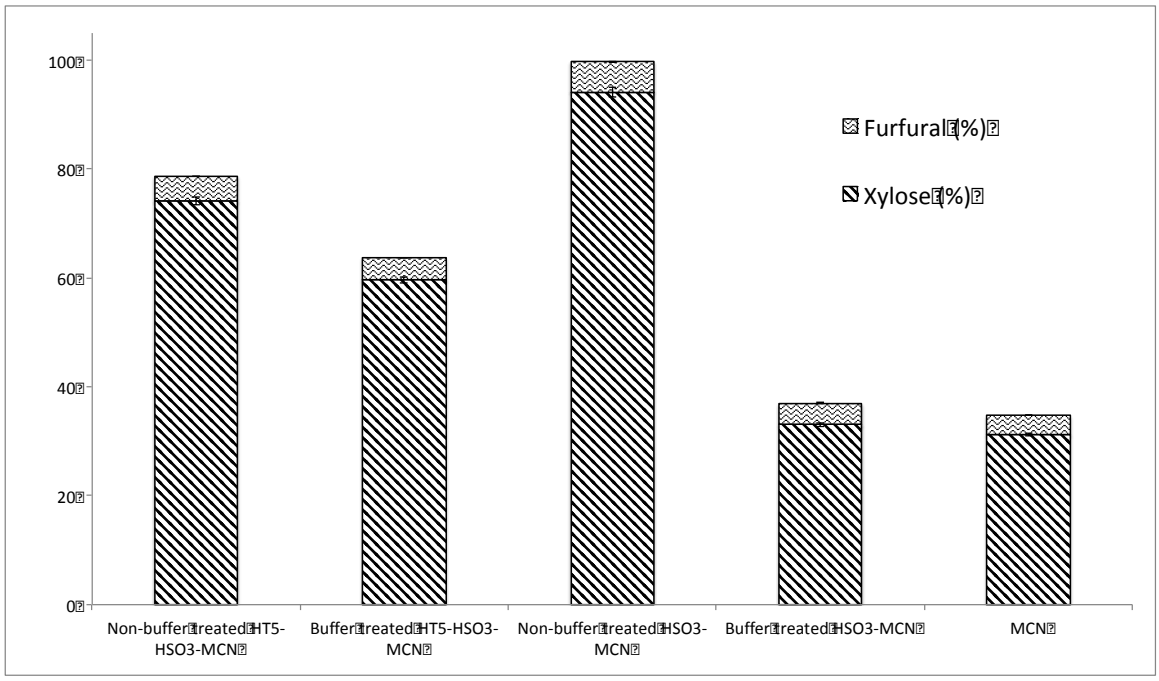

Figure S10. Comparison of hydrolysis of xylan using buffer-pretreated functional mesoporous carbon materials. Experimental details: acetate-buffer pretreatment of the HT_5-HSO_3-MCN and HSO_3-MCN materials was performed by separately treating 25 mg of each MCN-based material with 25 mL of 0.02 M sodium acetate buffer (under vortex for 1 h and subsequently filtering, washing with 5 mL of deionized water, and drying), before treatment with xylan-extract and acetate buffer solutions, and finally subsequent hydrolysis reaction in the acetate-buffered xylan extract.

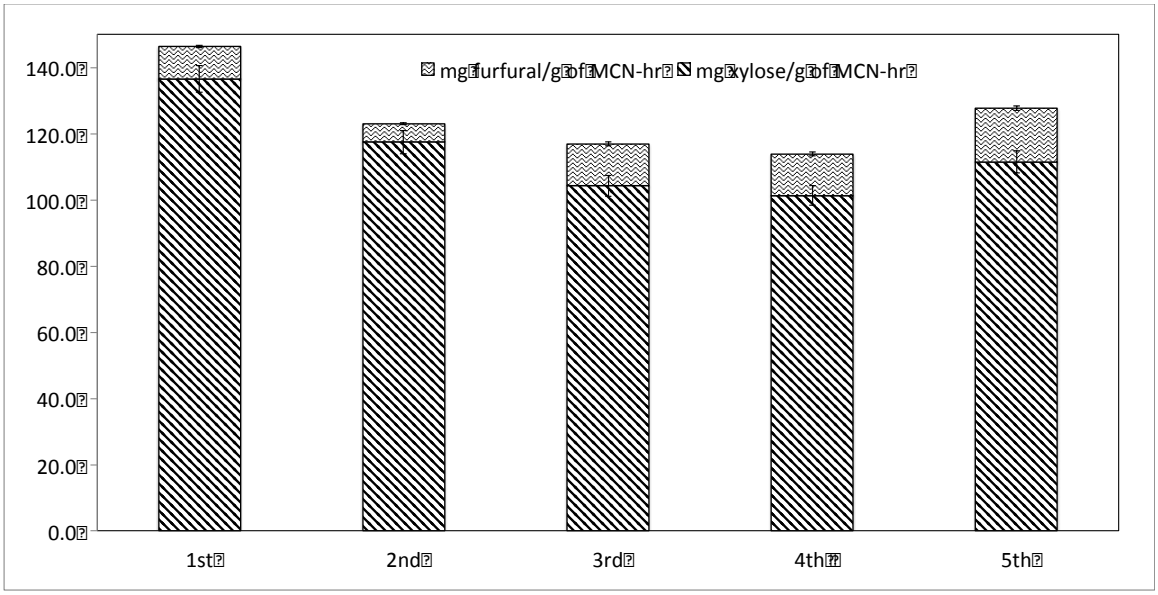

Figure S11. Recycle study of using HT_1-HSO_3-MCN. Experimental: 10 mg of material was washed with 5 mL of 0.1 M NaOH in 50:50 v/v EtOH/H_2O, 5 mL of EtOH, 20 mL of deionized water, 3 mL of 4 M HCl, and 30 mL of deionized water, and dried before reuse for xylan hydrolysis in *Miscanthus* xylan extract.

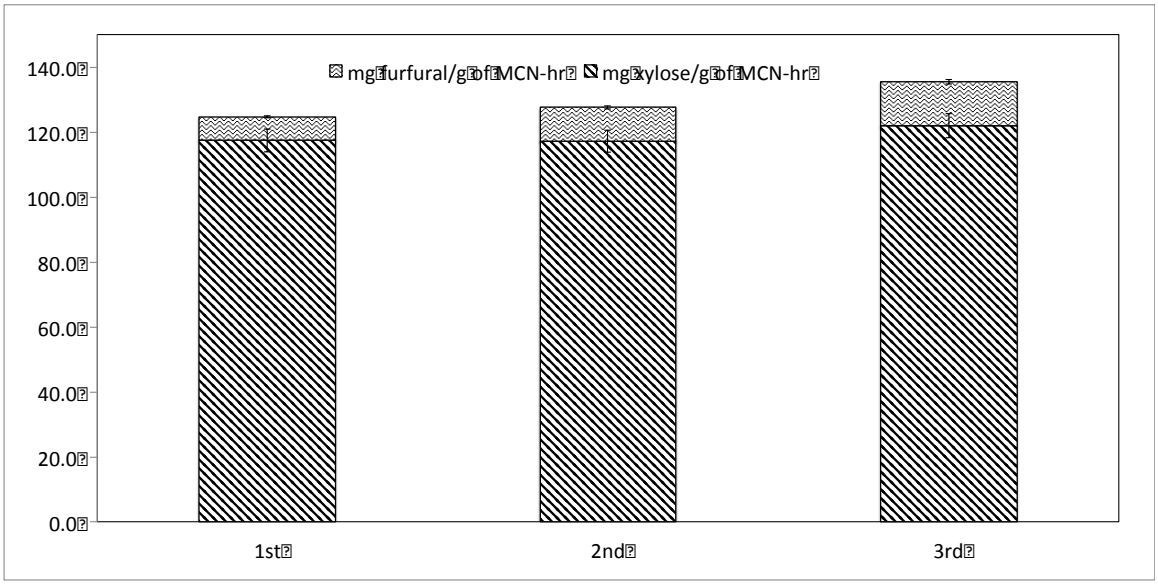

Figure S12. Recycle study of using HT_5-HSO_3-MCN. Experimental: 10 mg of material was washed with 5 mL of 0.1 M NaOH in 50:50 v/v EtOH/H_2O, 5 mL of EtOH, 20 mL of deionized water, 3 mL of 4 M HCl, and 30 mL of deionized water, and dried before reuse for xylan hydrolysis in *Miscanthus* xylan extract.

Lack of Directly Proportional Correlation Between Phenolic OH Surface Coverage and Hydrolysis Catalysis Rate

In general, weak-acid sites consist of phenolic OH and carboxylic acid functionality. The total number (per unit mass) of weak-acid sites in HT_5-HSO_3-MCN is 2.4-fold higher than in untreated MCN. With x being the total number (per unit mass) of weak-acid sites in untreated MCN, the maximum number of phenolic OH functionality in HT_5-HSO_3-MCN would be 2.4x, assuming no weak-acid site catalysis contribution from carboxylic acids (no carboxylates observed by ATR-FTIR results in Figure 3) in this material. If the phenolic OH group is the active site responsible for hydrolysis catalysis, there would have to be a maximum of 0.34x (or 7-fold less than 2.4x, since the rate enhancement over background for HT_5-HSO_3-MCN versus MCN is 7-fold) phenolic OH surface-functional groups in untreated MCN. This would require 0.66x of weak acid sites in untreated MCN to be carboxylic acid functionality. However, such a high proportion (1.94-fold higher number density) of carboxylic acid to phenolic OH sites in material MCN is impossible given ATR-FTIR results in Figure 3, which show no evident carbonyl band for material MCN (compare with material COOH-MCN) relative to OH bands. This means that, in order to be consistent with ATR-FTIR results, the number of phenolic OH groups must be considerably larger than 0.34x. However, such an outcome would require only a fraction of phenolic OH groups as the active site in both materials, since the 7-fold increase in catalytic activity observed for HT_5-HSO_3-MCN versus untreated MCN would require more than the measured 2.4x of total weak-acid sites in HT_5-HSO_3-MCN. Such an impossibility precludes a scenario where each phenolic OH groups is an active site responsible for the observed xylan hydrolysis catalysis. This suggests that a “special”

OH group – organized in a particular way as a minority species (as described in the manuscript) – is actually the active site.